Exchange–correlation thermal effects in shocked deuterium: Softening the principal Hugoniot and thermophysical properties

V.V. Karasiev,* S.X. Hu, M. Zaghoo, and T.R. Boehly
Laboratory for Laser Energetics, University of Rochester, 250 East River Road, Rochester, New York 14623-1299, USA
(Dated: original 27 FEB 2019; 03 JUN 2019, Rev. 1)

Exchange–correlation (XC) thermal effect for transport and optical properties of deuterium along the principal Hugoniot are investigated. The study is performed using *ab initio* molecular dynamics simulations within the Mermin–Kohn–Sham density functional theory. XC thermal effects are taken into account via the temperature-dependent Karasiev Dufty Trickey (KDT16) generalized gradient approximation functional [Phys. Rev. Lett. **120**, 076401 (2018)]. We find that XC thermal effects account for the softening of the Hugoniot at pressures $P > 250$ GPa and improve agreement with recent experimental measurements. Also, XC thermal effects lead to the reflectivity increase by about 2% for shock speeds above 20 km/s. Calculated reflectivity for shock speeds up to 50 km/s is in excellent agreement with recent experimental measurements on the OMEGA Laser System. The dc conductivity is increased by about 4% due to XC thermal effects. The system evolution along the Hugoniot crosses the so-called warm-dense-matter regime, and XC thermal effects must be taken into account to accurately predict the thermophysical properties across warm dense conditions.

PACS numbers:

I. INTRODUCTION

Reliably predicting the properties of hydrogen and its isotopes under extreme conditions remains a problem of great importance and broad scientific interest. Accurate knowledge of the equation of state (EOS) and transport properties over a wide range of thermodynamic conditions of this simplest and most-abundant element in the universe is used as input for planetary, brown dwarf and stellar modeling [1] as well as the inertial confinement fusion (ICF) simulations to design targets [2–4]. The most-advanced theoretical and computational methods are used to interpret experimental results and to predict properties at thermodynamic conditions that are difficult to access experimentally.

On the other hand, new experimental measurements with improved accuracy [5, 6] serve as an important benchmark to assess the accuracy of theoretical predictions. It was found [6] that recent shock-compression data for deuterium are well described by finite-temperature density functional theory (DFT) methods [7–9] and are in disagreement with recent quantum Monte Carlo (QMC) results [10]. The QMC method [10] fails to correctly describe the shock compression near the molecular-to-atomic (MA) transition for both the onset of dissociation and peak compression [6]. DFT calculations with exchange–correlation (XC) functionals that account for van der Waals (vdW) long-range interactions (vdW-DF1 [11] and vdW-DF2 [12]) provide an improved description of the onset of the dissociation process along the Hugoniot, while peak compression is underestimated by these functionals. Standard generalized gradient approximation (GGA) XC functionals such as Perdew–Burke–Ernzerhof (PBE) [13] describe the peak compression reasonably well, but the dissociation process begins at a slightly (∼3-GPa) lower pressure as compared to the experimental data (see details in Ref. [6]). At pressures above 250 GPa along the Hugoniot, the DFT calcu-

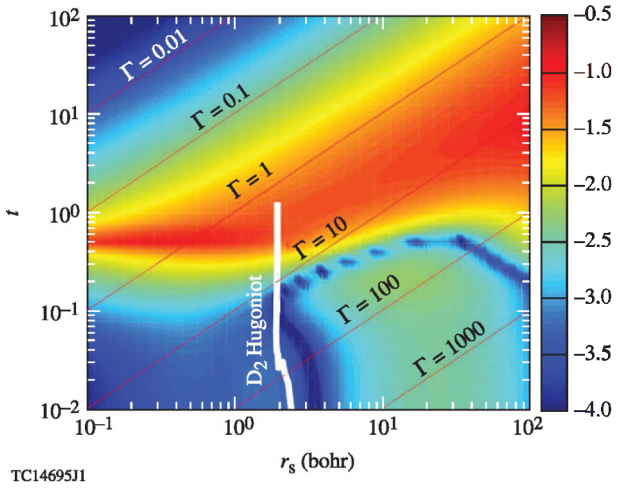

FIG. 1: The relative importance of explicit temperature dependence in the XC free-energy functional for the homogeneous electron gas measured as $\log_{10}\left[|f_{\rm xc}(r_{\rm s},t) - e_{\rm xc}(r_{\rm s})|/[|f_{\rm s}(r_{\rm s},t)|+|e_{\rm xc}(r_{\rm s})|]\right]$, where $f_{\rm xc}$ is the XC free-energy per particle given by the corrected Karasiev–Sjostrom–Dufty–Trickey (corrKSDT) parameterization [24, 25], $e_{\rm xc}$ is the zero-temperature XC energy per particle [26], and $f_{\rm s}$ is the non-interacting free energy per particle [27]. $\Gamma = 2\lambda^2 r_{\rm s}/t$ with $\lambda = (4/9\pi)^{1/3}$ is the classical coupling parameter. The solid white line corresponds to the liquid deuterium principal Hugoniot path; the end point corresponds to $P = 1$ TPa.

*Electronic address: vkarasev@lle.rochester.edu

lations with the PBE functional predict a stiffer behavior than recent experimental data [5].

Furthermore, optical and transport properties such as reflectivity, thermal conductivity, and electrical conductivity are important material properties used to characterize the complex behavior of shocked deuterium, which includes, in particular, insulator-to-metal and degenerate-to-nondegenerate plasma transitions. *Ab initio* molecular dynamics (AIMD) simulations, when the classical molecular dynamics for the ionic degrees of freedom is combined with the DFT treatment for the electrons, take into account quantum effects and treat all electronic thermally occupied and empty states on the same basis. All of this is important to accurately predict transport coefficients via Kubo–Greenwood formalism [14, 15], especially in the partially degenerate, strongly coupled regime when the chemical- and plasma-based models [16, 17] become inaccurate [4].

All current DFT calculations of the Hugoniot data and transport coefficients are performed with temperature-independent XC functionals developed for ground state [4, 6, 18–21]; therefore, XC thermal effects, which play an important role at warm-dense-matter (WDM) conditions [22], are not taken into account. Figure 1 shows the (r_s, t) domain where the T dependence of XC might be important for accurate predictions. The relative importance of XC thermal effects is shown as a function of the Wigner–Seitz radius $r_s = (3/4\pi n)^{1/3}$ and reduced temperature $t = T/T_F$ [$T_F = [3\pi^2 n]^{2/3}/2k_B$ is the Fermi temperature and n is the electron number density]. At low-r_s XC thermal effects might become important for t values between a few tenths and $t \approx 1$; at large-r_s the interval is expanded up to $t \approx 10$ or even higher. At high density (low-r_s) and high temperatures the exchange-correlation does not play any role (see Fig. 1 in Ref. 23), and XC thermal effects become negligible as well. At low densities the relative magnitude of the XC term with respect to the non-interacting piece is increased, therefore one may expect that XC thermal effects might be noticeable even at lower temperatures (light blue and dark green zone at $r_s \geq 10$ and low-t in Fig. 1). For deuterium, the reduced temperature reaches a value of 0.1 at pressures near 70 GPa along the principal Hugoniot; therefore, we expect that XC thermal effects might be important for pressures beyond this value.

Here we focus on the study of the optical and transport properties along the principal Hugoniot of deuterium with a temperature-dependent Karasiev–Dufty–Trickey (KDT16) generalized gradient approximation XC functional [24]. KDT16 in the zero-temperature limit by construction reduces to the standard ground-state PBE [13]. Therefore, a second set of calculations is performed with the ground-state PBE XC to assess the XC thermal effects calculated as the difference between the two sets of results for several thermophysical properties.

The next section provides details of the methodology used in this study including computational details. Section III describes our main results, and Sec. IV provides a short summary and conclusions.

II. METHOD

A. Exchange–correlation free-energy functional

Treatment of electronic degrees of freedom via the finite-temperature DFT requires the use of an approximate XC free-energy functional. The reliability of the DFT predictions at high-energy-density (HED) conditions depends crucially on having an XC free-energy functional that is accurate across temperature regimes. Reference 22 studied XC thermal effects at the local density approximation (LDA) level of refinement and found that temperature-dependent Karasiev–Sjostrom–Dufty–Trickey (KSDT) XC functional [25] in particular yields improved agreement with experiment for the dc electrical conductivity of low-density aluminum (Al).

For nonhomogeneous systems it is important to go beyond the LDA and take into account the XC nonhomogeneity and thermal effects simultaneously via the nonempirical KDT16 GGA XC free-energy functional [24]. The KDT16 functional is constrained by the correct temperature dependence in the slowly varying regime and the correct zero-temperature, high-temperature, and homogeneous electron gas limits. The correct zero-temperature limit means that the KDT16 at $T = 0$ reduces by construction to the extremely widely used ground-state PBE functional [13]. The KDT16 uses the corrected KSDT (corrKSDT) parametrization as the LDA component. In this work we use the KDT16 XC free-energy functional in such a way that all the XC thermal and nonhomogeneity effects are taken into account at the generalized gradient level of approximation. The KDT16 XC free energy is given as an explicit temperature-dependent functional of density, $\mathcal{F}_{xc}[n, T]$. Hugoniot calculations considered in Sec. III A require a knowledge of XC internal-energy contribution, which is calculated via standard thermodynamic relations for the XC entropy

$$\mathcal{S}_{xc}[n, T] = -\frac{\partial \mathcal{F}_{xc}[n, T]}{\partial T}\Big|_{N,V} \tag{1}$$

and internal energy

$$\mathcal{E}_{xc}[n, T] = \mathcal{F}_{xc}[n, T] + T\mathcal{S}_{xc}[n, T]\,. \tag{2}$$

The derivative with respect to temperature at a constant number of particles and system volume in Eq. (1) is calculated analytically, and functionals Eqs. (1) and (2) are evaluated together with $\mathcal{F}_{xc}$ while solving the Mermin–Kohn–Sham DFT equations.

Calculations with the ground-state PBE, when the XC free energy is approximated by a ground-state functional without explicit T dependence, $\mathcal{F}_{\rm xc}[n,T] \approx \mathcal{E}_{\rm xc}[n]$, are also performed to assess the magnitude of XC thermal effects on calculated properties. It is important to note that only temperature-dependent XC functionals provide explicit $\partial\mathcal{E}_{\rm xc}[n,T]/\partial T|_V$ contribution into the system's specific heats.

B. Computational details

AIMD simulations are performed in the canonical ensemble by using the ground-state PBE and temperature-dependent KDT16 XC functionals as implemented in the PROFESS@QUANTUMESPRESSO interface [28–31]. The electron–ion interaction was treated by a standard projector augmented wave (PAW) pseudopotential data set [32] generated at $T = 0$ K with the ground-state PBE XC. Such a PAW data set is compatible with the temperature-dependent KDT16 functional because the KDT16 functional, by construction, reduces to PBE in the zero-temperature limit at which the PAW set was generated. The underlying assumption, common in WDM studies, that effective electron–ion interaction potentials generated at zero-temperature are transferable to various thermodynamic conditions was confirmed for hydrogenic systems by comparison between the exact bare Coulomb and pseudopotential (given by simple local form) calculations (see Fig. 5 in Ref. 33 and studies of the PAW transferability to high density/temperature regimes in Ref. 34). Additionally we performed AIMD simulations at two representative temperatures (50 and 100 kK) near the maximum of the absolute and relative XC thermal effects on pressure (see Fig. 4 in Sec. III A) with use of our PAW data set and the exact electron–ion interaction given by the bare Coulomb potential. The agreement between calculations with the PAW and bare Coulomb interactions, shown in Table I is excellent: the largest pressure difference of 0.4 GPa is only 0.7 % of the electronic pressure and is much smaller compared to the pressure differences of 7 and 16 GPa (relative difference of 12% and 10% respectively) due to the XC thermal effects on pressure at $T = 50$ and 100 kK respectively. These calculations confirm transferability of the PAW data set generated at $T = 0$ K to finite temperatures.

Calculations were performed for a range of temperatures between 6000 K and 200,000 K. For each temperature, the AIMD simulations were performed for three densities to find solution of the Rankine–Hugoniot equation (see Sec. III A). The ion temperature was controlled by an Andersen thermostat and the electron temperature, set equal to that of ions, was fixed according to the Fermi-Dirac statistics. At low temperatures ($T \leq$ 20,000 K), calculations included 256 atoms in the supercell and Baldereschi's mean value point (BMVP) [35]. The size of the supercell gradually decreased to 128 atoms (for 25,000 K $\leq T \leq$50,000 K using BMVP), 64 atoms (for 50,000 K $\leq T \leq$75,000 K using BMVP and for 80,000 K $\leq T \leq$150,000 K using Γ point only), and 32 atoms for $T =$200,000 K using Γ point only. Additionally at temperatures $T = 75$, 100, and 150 kK we performed simualtions with 128 atoms and Γ point only to assess the magnitude of finite-size effects as compared to calculations with 64 atoms in simulation cell.

TABLE I: Electronic pressure from AIMD simulations with the PBE and KDT16 XC functionals and with use of the PAW and bare Coulomb external (electron–ion) potentials for deuterium at material density $\rho_{\rm D} = 0.7224$ g/cm^3 (64 atoms in simulation cell, (1/4,1/4,1/4) and Γ point only for $T = 50$ and 100 kK respectively).

$v_{\rm ext}$	T(kK)	$P^{\rm PBE}$(GPa)	$P^{\rm KDT16}$(GPa)
PAW	50	62.9	56.2
bare Coulomb	50	63.3	56.6
PAW	100	170.0	154.0
bare Coulomb	100	170.4	154.1

A sample set of 5 to 20 statistically independent configurations was selected from the AIMD ionic trajectories (so-called "snapshotting"). For this set of snapshots, a single-point DFT calculation was performed with the ABINIT [36] and/or PROFESS@QUANTUMESPRESSO [28] to generate a set of electronic-state functions $\{\psi_n\}$. For selected configurations we also performed calculations with the PROFESS@QUANTUMESPRESSO [28] to ensure that the results obtained from the two different codes (the DFT and the subsequent Kubo–Greenwood ones are in agreement). The velocity dipole matrix elements $\langle\psi_n|\nabla|\psi_m\rangle$ were used by post-processing codes from Ref. 37 for ABINIT and from Ref. 38 for PROFESS@QUANTUMESPRESSO to calculate the frequency-dependent Onsager coefficients within the Kubo–Greenwood formalism [14, 15] and eventually to calculate the real part of the dc and dynamic electrical conductivity [$\sigma_{\rm dc}$ and $\sigma(\omega)$, respectively], the electronic thermal conductivity $\kappa(\omega)$, the real and imaginary parts of the refractive index [$n(\omega)$ and $k(\omega)$, respectively], the reflectivity, and eventually the Rosseland mean opacity and specific heat. Calculation of the thermophysical properties including opacity with use of the Kubo–Greenwood formalism in combination with the AIMD snapshotting is a well established procedure frequently used at extreme HED conditions [39–43].

The reflectivity is defined as

$$r(\omega) = \frac{[n(\omega) - n_0]^2 + k^2(\omega)}{[n(\omega) + n_0]^2 + k^2(\omega)}\,, \qquad (3)$$

where n_0 is the refractive index of the ambient environment (deuterium in the initial liquid state in the case of the reflectivity calculations along the principal Hugoniot). Near maximum compression in the temperature range of 6 to 15 kK, these calculations were performed for a fixed density of 0.7568 g/cm^3 (4.4-fold compression); for $T \geq 20$ kK, a density of 0.7224 g/cm^3 (4.2-fold compression) was used (although small variations in material density have little effect on calculated properties). The δ function in the real part of the electrical conductivity, $\sigma(\omega)$, obtained using the Kubo–Greenwood formalism, is approximated by a Gaussian of width Δ (see Ref. 38 for details). We find that results are stable for Δ width in the range of a few tenths of eV; therefore, in our calculations $\Delta = 0.5$ eV was used. Convergence with respect to the number of snapshots was tested for selected points by increasing this number by a factor of two. Results for reflectivity and dc conductivity changed by 0.5% or less. Convergence of the reflectivity and dc conductivity with respect to the cell size was tested for two temperatures, $T = 20$ and 50 kK, by increasing the number of atoms from 128 to 256. The results are shown in Figs. 6 and 8, changes do not exceed 0.5% as compared to calculations with 128 atoms.

All simulations employed a plane-wave cutoff energy of 125 Ry to converge high-energy thermally occupied bands required for calculations at elevated temperature and Baldereschi's mean value point [35] or Γ-point sampling of the first Brillouin zone in the case of AIMD simulations and up to $3\times3\times3$ Monkhorst–Pack k-grid [44] for Kubo–Greenwood calculations. To ensure convergence with the number of bands, we used a minimum Fermi–Dirac occupation number threshold of the order of 10^{-6} to 10^{-7}.

It is important to notice that the KDT16 functional, employed in this work, is implemented in locally modified versions of the two codes, such that XC thermal effects are taken into account in both, the AIMD simulations providing "structural" properties and in the Kubo–Greenwood calculations providing transport properties.

III. RESULTS

A. The principal Hugoniot of deuterium up to 1 TPa

The Hugoniot curve is described by solutions of the Rankine–Hugoniot equation

$$\mathcal{E} - \mathcal{E}_0 - \tfrac{1}{2}(P + P_0)\Big(\frac{1}{\rho} - \frac{1}{\rho_0}\Big) = 0\,, \qquad (4)$$

where $\mathcal{E}$, P, and ρ are the specific *internal* energy, pressure, and bulk density, respectively, of a state derived by single-shock compression from an initial state at ρ_0, $\mathcal{E}_0$, and P_0. We performed an AIMD simulation for liquid deuterium at initial conditions $\rho_0 = 0.172$ g/cm^3, $T_0 = 20$ K with 32 D_2 molecules in a simulation cell and obtained an average pressure P_0=0.15 kbar, which is negligible in comparison to the final pressure P. The difference between the average energy per molecule from the AIMD simulation and the energy of isolated D_2 molecule (single molecule in large simulation box) is only 0.006 eV. Therefore, an AIMD simulation for the initial state is not required unless one is interested in corresponding optical properties. In this work the initial-state AIMD snapshots were used to calculate the real part of the refractive index n_0 required for reflectivity calculations [Eq. (3)] (see Sec. III B). The AIMD snapshot and radial distribution function (RDF) shown in Fig. 2 confirm that the initial state represents pure D_2 molecular liquid. The RDF has a very sharp peak at the D_2 molecule equilibrium distance $r \approx 1.4$ bohr and a small tail starting at a relatively large $r \approx 4.5$-bohr distance.

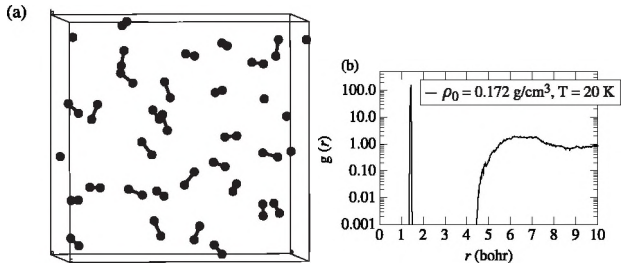

FIG. 2: AIMD snapshot of liquid deuterium at initial conditions (a) and radial D–D distribution function (b).

The deuterium principal Hugoniot was calculated from simulations with the KDT16 and PBE XC functionals. Calculations were performed over the temperature range of 6 kK ($P = 34$ GPa, near the MA transition) to 200 kK ($P = 1010$ GPa). Figure 3 compares our theoretical predictions, experimental results across the MA transition (low-pressure range $P < 150$ GPa) [6] shown as the blue diamonds, and recent experimental measurements over the high-pressure range between 87 to 550 GPa [5] shown as the orange circles. The KDT16 and PBE curves [obtained by combining results from simulations with 256, 128, 64, and 32 atoms (see Fig. 3 caption and Sec. II B)] are indistinguishable up to a relatively high temperature $T = 60$ kK ($P \approx 250$ GPa).

According to Fig. 1, XC thermal effects might become noticeable starting at a lower temperature $\sim 0.2T_{\rm F}$. Figures 4(a) and 4(b) show pressure and specific internal energy differences between KDT16 and PBE, $\Delta P = P^{\rm KDT16} - P^{\rm PBE}$ and $\Delta\mathcal{E} = \mathcal{E}^{\rm KDT16} - \mathcal{E}^{\rm PBE}$ along the Hugoniot. These differences represent XC thermal effects on pressure and energy and, as functions of T, have the same sign: negative for $T < 250$ kK and positive for $T > 250$ kK. Consequently, the differences effectively cancel out in the left-hand side of Eq. (4), the solution

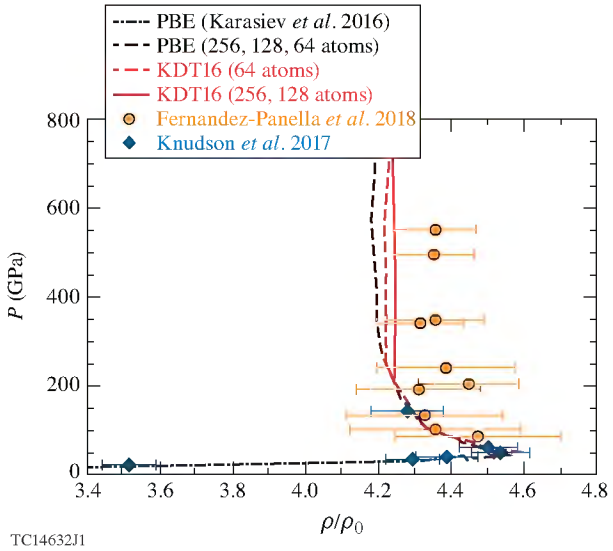

FIG. 3: Deuterium principal Hugoniot derived from the initial state $\rho_0 = 0.172$ g/cm^3 and $T_0 = 20$ K. The PBE (black dashed) and KDT16 (red dashed) curves are obtained by combining results from simulations with 256 atoms ($6 \le T \le 20$ kK, pressure range between 34 and 86 GPa for both functionals), 128 atoms ($25 \le T \le 50$ kK, pressure range between 104 and 208 GPa for KDT16), 64 atoms ($60 \le T \le 150$ kK, pressure range between 253 and 736 GPa for KDT16), and 32 atoms for $T = 200$ kK. The red solid curve corresponds to the KDT16 results from simulations with 256 atoms ($6 \le T \le 20$ kK) and 128 atoms ($25 \le T \le 150$ kK).

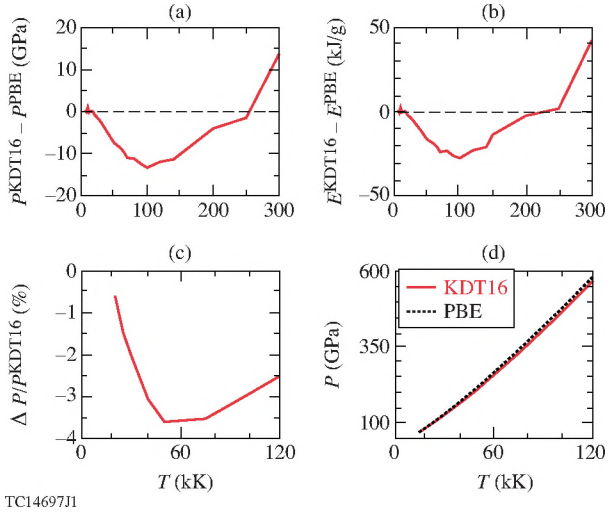

FIG. 4: Pressure (a) and specific internal energy (b) differences; relative pressure difference $[(P^{\mathrm{KDT16}} - P^{\mathrm{PBE}})/P^{\mathrm{KDT16}} \times 100\%]$ (c) and total pressure (d) along the deuterium Hugoniot as functions of temperature.

of which remains unchanged for $T < 60$ kK. The Hugoniot curve's similar insensitivity to the use of the LDA temperature-dependent XC functional rather than the ground-state LDA XC was previously observed in Ref. [22]. In spite of the Hugoniot curve (pressure versus compression) being weakly affected by XC thermal effects (due to effective cancellation between the energy and pressure terms as just discussed), the pressure along the Hugoniot is lowered because of XC thermal effects and the relative pressure difference reaches about 4% at T near 50 kK [see Figs. 4(c) and 4(d)].

Back to discussing Fig. 3, both functionals, KDT16 and PBE, are in good agreement with experimental measurements in the range of pressure up to 200 GPa [6]. At higher pressures, however, the PBE curve becomes noticeably stiffer as compared to the recent experimental data [5]; the disagreement reaches about 4% at $P = 550$ GPa. The KDT16 predicts a curve that is softer by slightly more than 1% beyond 250 GPa as compared to PBE. Increasing the simulation cell size from 64 to 128 atoms in this range of pressure leads to further softening of the Hugoniot. Simulations with 128 atoms at $T > 50$ kK computationally are very demanding, so only calculations with KDT16 functional were performed, and XC thermal effects in this range of pressure are estimated from simulations with 64 atoms. Calculated KDT16 and experimental compression does not vary in this range of P. The KDT16 compressibility is within the experimental uncertainty in the entire pressure range (including high pressures $P > 250$ GPa). Therefore, the inclusion of XC thermal effects in AIMD calculations makes the deuterium Hugoniot softer at $P > 250$ GPa and improves agreement with the experimental data. Reference 5 found that good agreement with the experimental data for low pressure $P < 200$ was observed for the PBE DFT predictions and for a range of pressure between 200 and 550 GPa was observed for the two models: the chemical LEOS 1014 model [45] and the FPEOS model [2], which in this range of P is based on the path-integral Monte Carlo (PIMC) simulations; the authors concluded that no single model consistently describes the deuterium principal Hugoniot throughout the entire pressure range. The KDT16 Hugoniot curve at low pressure is identical to the PBE curve and at high pressure has the quality of the PIMC FPEOS model. Therefore, by including XC thermal effects in consideration, the KDT16 XC functional is able to describe the principal Hugoniot of liquid deuterium consistently over the entire pressure range.

B. Thermophysical properties

Deuterium along the principal Hugoniot experiences changes in material structure that can, in turn, change the thermophysical properties such as dc and dynamic electrical conductivity, reflectivity, and thermal conductivity. Reduced temperature (degeneracy parameter) along the Hugoniot changes between $3 \cdot 10^{-4}$ (degenerate

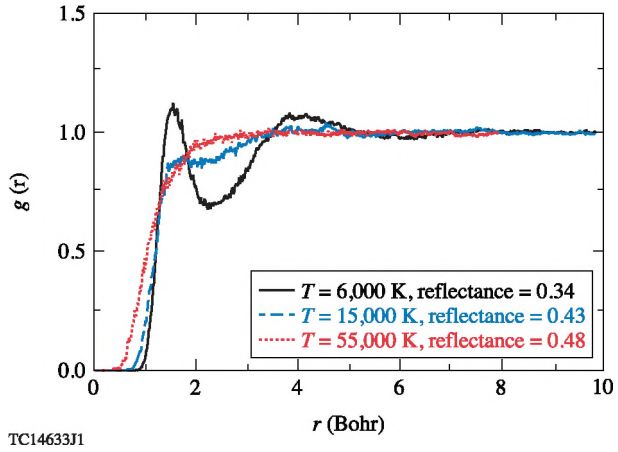

FIG. 5: Radial distribution function for a few selected temperatures along the deuterium Hugoniot.

limit) and 1 (nondegenerate classical system) (see Fig. 1). The range of classical coupling parameter Γ is between 5000 (strongly coupled) and near 1 (moderately coupled). Consequently, the system's evolution occurs across a wide range of degeneracy and coupling parameters, from degenerate strongly coupled quantum to nondegenerate moderately coupled classical regimes.

Figure 5 illustrates structural changes. A relatively broad peak near 1.5 bohr presented at $T = 6$ kK indicates that the system is still a molecular liquid with the D_2 bond-length range of ∼1.2 to 1.8 bohr but the dissociation process is in progress. At $T = 15$ kK, the molecular-to-atomic transition is already completed (see Ref. 6), even though some long-range order remains. This structural change leads to a significant increase in reflectivity (from 0.34 to 0.43; details to be discussed in below). Further evolution of the system leads to a completely structureless radial distribution function and an increase in reflectivity. In this section we present our theoretical predictions for reflectivity, the dynamic and dc electrical conductivity, thermal conductivity, the Lorentz number, the Rosseland mean opacity, and specific heat along the deuterium principal Hugoniot performed within the DFT and Kubo–Greenwood formalism by using the standard ground-state PBE XC and temperature-dependent KDT16 XC to assess the role of XC thermal effects.

Figure 6(a) presents reflectivity as a function of the shock speed calculated with the two XC functionals. As a result of XC thermal effects, the reflectivity is increased by about 2% for shock speeds above 20 km/s ($T > 12$ kK). Figure 6(b) presents the real part of the index of refraction n_0 of liquid deuterium in the initial state ($\rho_0 = 0.172$ g/cm^3 and $T = 20$ K) as a function of photon frequency. The refractive index is flat at low ω and takes a value of 1.17 at 532 and 808 nm, the probe wavelengths used in experiments. This result is in good agreement with the reference value of 1.14 [46]. To compare with the experimental data, the reflectivity was calculated at 532 and 808 nm with the KDT16 XC functional and our predicted value of the refractive index. Results of recent experiments [47] on OMEGA and previous measurements [48] are shown in Fig. 7. There is excellent agreement between the KDT16 values and experimental data at 808-nm wavelength for the range of shock speeds considered in calculations, even though the experimental data have relatively large error bars. The KDT16 results at 532 nm are in very good agreement with recent OMEGA experimental data for shock speeds below 50 km/s. The reflectivity is underestimated by the DFT calculations at high shock speeds $U_s > 50$ km/s as compared to the experiment. Experimental reflectance as a function of shock speed changes the slope at U_s near 45 km/s ($T \approx 0.4T_F = 60$ kK); this change of the slope is related to lifting of the Fermi degeneracy. The system starts to behave as a classical one at a significantly lower temperature as compared to T_F (see details in Ref. [47]). Calculated KDT16 reflectivity at the same 532-nm wavelength rises very quickly from 0.29 at 16 km/s ($T \approx 6$ kK) to 0.39 at 20 km/s ($T \approx 12$ kK), which roughly corresponds to maximum compression near molecular-to-atomic transition; it slowly continues to increase and near 43 km/s the slope also increases. This qualitative behavior of DFT predictions is in agreement with the experimental data, but the experimental data slope increase is larger. Our PBE reflectivity data (not shown in Fig. 7) lie slightly lower as compared to the KDT16 curve [see Fig. 6(a)] and the agreement with experiment is a bit worse. Figure 7 also shows PBE results of previous studies [4, 21] that observed a similar change of the reflectivity slope at a shock speed near 45 km/s. These calculations used $n_0 = 1$ value; as a consequence the reflectivity at 532 nm is overestimated in comparison with experimental measurements.

To gain further insights into the properties of the shocked deuterium, the dc electrical conductivity, thermal conductivity, Lorentz number, Rosseland mean opacity, and specific heat were calculated. The four panels in Fig. 8 show the results. Using the temperature-dependent exchange correlation has an effect on the dc electrical conductivity: σ_{dc} is increased by 4% at intermediate shock speeds between 25 and 40 km/s. The dc conductivity is increasing very fast across the molecular-to-atomic transition (the U_s range is ≈ 16 to 20 km/s; T range is between 6 and 12 kK) similar to the reflectivity increase shown in Fig. 7. After reaching the maximum at the end of the molecular-to-atomic transition, the system behaves as a liquid metal: σ_{dc} decreases with an increase in temperature for U_s between 20 and 30 km/s (T between 12 and 30 kK). For $U_s > 30$ km/s ($T > 30$ kK), the electrical dc conductivity increases with temperature as in the plasma regime, which is consistent with an observed degenerate-to-nondegenerate plasma

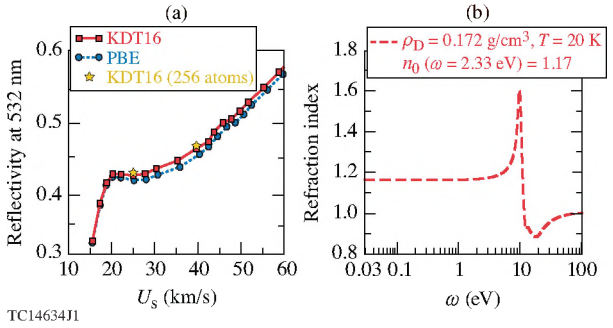

FIG. 6: Reflectivity (for a wavelength of 532 nm) along the deuterium Hugoniot as a function of the shock speed calculated with the ground-state PBE and temperature-dependent KDT16 XC functionals by using Eq. (3) and $n_0 = 1$ (a) and the real part of the refractive index for liquid deuterium in initial state (b). The reflectivity curves are obtained by combining results from simulations with 256 atoms ($16 \le U_s \le 22$ km/s), 128 atoms ($25 \le U_s \le 42$ km/s), and 64 atoms ($44 \le U_s \le 75$ km/s).

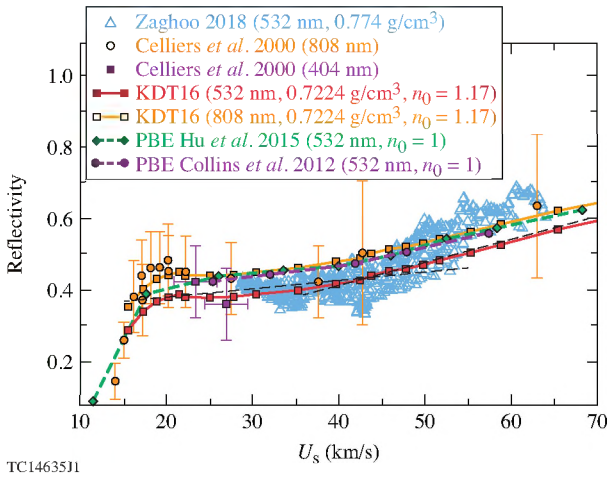

FIG. 7: Reflectivity of shocked deuterium. Theoretical DFT predictions and experimental data are compared.

transition [47]. Thermal conductivity κ is practically identical for calculations with ground-state and finite-temperature XC functionals; κ increases with slight increase of temperature dependence at $T \approx 60$ kK, κ behaves as $\kappa \propto T^{1.6}$ at $T \gtrsim 0.4T_F = 60$ kK. The Lorentz number, defined as a ratio $L = \kappa/\sigma_{dc}T$, is close to the degenerate limit value of 2.44 $\times 10^{-8}$ given by the Wiedemann–Frantz law at U_s near 20 km/s and grows with temperature. At $U_s \approx 43$ km/s, this trend is reversed, and at high shock speeds (high temperatures), the Lorentz ratio approaches the nondegenerate classical limit.

The Rosseland mean opacity is shown in Fig. 8(d) as a function of temperature. At intermediate temperatures, it behaves according to Kramers law (shown by black

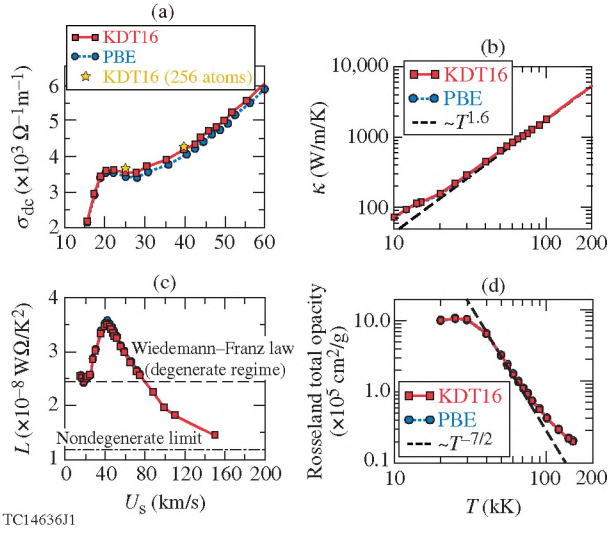

FIG. 8: The dc electrical conductivity (a), thermal conductivity (b), Lorentz number (c), and Rosseland mean opacity (d) along the deuterium Hugoniot as functions of the shock speed (dc conductivity and Lorentz number) or as as function of temperature (thermal conductivity and opacity) calculated with the ground-state PBE and temperature-dependent KDT16 XC functionals. All curves are obtained by combining results from simulations with 256 atoms ($16 \le U_s \le 22$ km/s, T between 6 and 15 kK), 128 atoms ($25 \le U_s \le 42$ km/s, T between 20 and 55 kK), and 64 atoms ($44 \le U_s \le 75$ km/s, T between 60 and 150 kK).

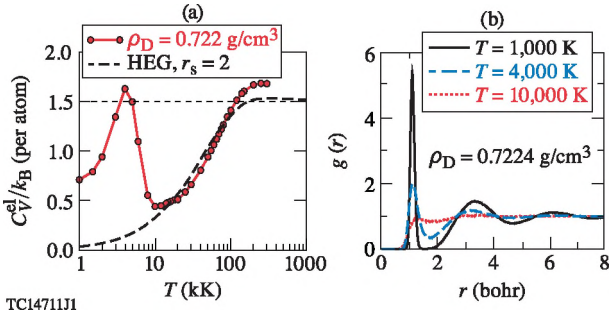

FIG. 9: The specific heat C_V^{el} (a) (in units of k_B per atom) as a function of temperature for deuterium at material density $\rho_D = 0.7224$ g/cm^3 calculated from AIMD simulation data (circles, solid line) and for the homogeneous electron gas (dashed line); and the radial distribution function for the three representative temperatures at $\rho_D = 0.7224$ g/cm^3 (b). All were calculated with the KDT16 XC functional.

dashed line) when bound-free and free-free contributions are dominating. At $T \approx 0.43T_F = 65$ kK ($U_s \approx 45$ km/s) it starts to deviate from $\sim T^{-7/2}$ behavior toward saturation when electron scattering is the dominant opacity contribution. Saturation is expected to occur at very high temperatures when the system is completely ionized.

Eventually Fig. 9(a) shows the heat capacity $C_V^{el} =$

$(\partial \mathcal{E}^{\rm el}/\partial T)_V$, where $\mathcal{E}^{\rm el}$ is the electronic structure internal energy

$$\mathcal{E}^{\rm el} = \mathcal{T}_{\rm s} + \mathcal{E}_{\rm H} + \mathcal{E}_{\rm xc} + \mathcal{E}_{\rm ion-el} + \mathcal{E}_{\rm ion-ion}\,, \qquad (5)$$

calculated from the AIMD simulation data for deuterium at material density $\rho_{\rm D} = 0.7224$ g/cm^3 ($r_{\rm s} = 2$) as a sum of noninteracting kinetic energy of electrons, electronic Hartree, electronic XC, ion–electron interaction, and ion–ion classical electrostatic interaction terms. Energy $\mathcal{E}^{\rm el}$ extracted from AIMD simulations was represented in the form of Padé approximants [49] by fitting on two temperature intervals, below and above 20 kK, to reduce fitting errors that unfortunately affect accuracy of results for $C_V^{\rm el}$. The total internal energy of the system is given by $\mathcal{E}_{\rm tot} = \mathcal{T}_{\rm kin-ion} + \mathcal{E}^{\rm el}$, where the classical kinetic energy of ions depends on (ionic) temperature T as $\mathcal{T}_{\rm kin-ion} = (3/2)Nk_{\rm B}T$, where N is the number of atoms. Therefore the ionic kinetic energy has a temperature-independent contribution to the heat capacity $C_V^{\rm ion-kin} = (3/2)k_{\rm B}$ per atom, and the total heat capacity is given by $C_V^{\rm tot} = (3/2)k_{\rm B} + C_V^{\rm el}$.

Results for the homogeneous electron gas (HEG) of the same density (same $r_{\rm s}$) are shown for comparison (dashed line in Fig. 9). At $T = 1$ kK, the system represents pure diatomic molecular liquid, $C_V^{\rm el} = 0.7k_{\rm B}$, and is increasing with an increase in temperature due to growing contribution of molecular vibrational degrees of freedom. $C_V^{\rm el}$ reaches a maximum in pre-dissociation state at $T = 4$ kK and drops down to a minimum after dissociation is over ($T \approx 10$ kK). Figure 9(b) shows RDF at these three representative temperature and illustrates that at $T = 1$ kK, the system is pure diatomic liquid, at $T = 4$ kK the dissociation process begins, and at $T = 10$ kK the dissociation is complete. At $T > 10$ kK the $C_V^{\rm el}$ behavior is very close to the HEG curve. This means that the pure electronic contribution to $C_V^{\rm el}$ is dominating after the molecular-to-atomic liquid transition ends at $T > 10$ kK. At high temperature ($T \geq 0.65T_{\rm F} = 100$ kK), the electronic contribution becomes close to the ideal gas value of $3/2k_{\rm B}$ per particle.

IV. SUMMARY AND CONCLUSIONS

In this work we studied the thermophysical properties of shocked deuterium along the principal Hugoniot up to 1 TPa by using the temperature-dependent XC functional within the Mermin–Kohn–Sham DFT and Kubo–Greenwood approach. It was found that inclusion of XC thermal effects leads to softening of the principal Hugoniot at high pressure $P > 250$ GPa, which improves agreement with recent experimental measurements. Although XC thermal effects on the Hugoniot curve (pressure versus compression) are reduced by an effective cancellation between the pressure and energy differences, the XC functional that included thermal effects provide a consistent description of the principal Hugoniot throughout the entire pressure range.

Changes in material structure and associated changes of reflectivity and the electrical conductivity along the deuterium Hugoniot qualitatively are consistent with previous studies [20, 21]. Quantitatively, however, the results are different. The magnitude of XC thermal effects on various properties is different. The reflectivity is increased by about 2% at intermediate temperatures above 12 kK, leading to a slightly better agreement with experiment (the KDT16 curve in Fig. 6 passes right through the middle of the experimental points for $U_{\rm s} < 50$ km/s). However the experimental error bars are larger than 2%, therefore the reflectivity without XC thermal effects taken into account will be within the error bars as well. The electrical dc conductivity is increased by 4% at intermediate temperatures, and, based on a previous study of dc conductivity in warm dense aluminum [22], we might expect that this increase goes in the right direction and improves reliability of theoretical predictions.

The deuterium system along the Hugoniot experiences transformations from an insulating molecular liquid to atomic poor metallic liquid and finally to nondegenerate classical plasma. The signature of the molecular-to-atomic transition is found in a sharp increase of electrical dc conductivity and reflectivity at shock speeds in the range between 16 and 20 km/s (a range of temperature between 6 and 12 kK). An increase in the slope of calculated reflectivity at $U_{\rm s} \approx 43$ km/s ($T \approx 0.4T_{\rm F} = 60$ kK), related to the breakdown of the electrons' degeneracy and emergence of classical statistics [47], is in agreement with experimental measurements. Thermal conductivity slightly changes behavior at the same temperature $T \approx 0.4T_{\rm F}$, although its temperature dependence $\kappa \propto T^{1.6}$ remains slow as compared to the ideal plasma limit $\kappa \propto T^{2.5}$. Rosseland mean opacity is another property that exhibits change in behavior toward classical system at $U_{\rm s} \approx 45$ km/s ($T \approx 0.43T_{\rm F} = 65$ kK). However, the electronic structure heat capacity $C_V^{\rm el}$, which at $T > 10$ kK is dominated by pure electronic contribution, approaches the classical $3/2k_{\rm B}$ value at a higher temperature $T = 0.65T_{\rm F} = 100$ kK. Electrical dc conductivity changes behavior and starts to increase with temperature as in the plasma regime at a shock speed slightly above 30 km/s (temperature above 30 kK). Our results confirm that the crossover between the quantum and classical statsitics occurs below the $T = T_{\rm F}$ limit. This is apparent in the observed change in the transport and the thermodynamic properties of the deuterium fluid in the region of 0.4–0.65 $T_{\rm F}$. Future work should investigate the dependence of the onset of this crossover on density.

The KDT16 functional takes into account XC thermal

effects at the GGA level of sophistication. This functional inherited limitations of it's zero-temperature PBE limit, in particular the limitation of the energy band-gap underestimation. Therefore development of more-advanced temperature-dependent GGA's and/or meta-GGA's based, for example, on deorbitalized meta-GGA [50] and also inclusion of the long-range van der Waals interaction [51] might provide a better description of thermophysical properties across the entire temperature–pressure range.

V. ACKNOWLEDGMENTS

This report was prepared as an account of work sponsored by an agency of the U.S. Government. Neither the U.S. Government nor any agency thereof, nor any of their employees, makes any warranty, express or implied, or assumes any legal liability or responsibility for the accuracy, completeness, or usefulness of any information, apparatus, product, or process disclosed, or represents that its use would not infringe privately owned rights. Reference herein to any specific commercial product, process, or service by trade name, trademark, manufacturer, or otherwise does not necessarily constitute or imply its endorsement, recommendation, or favoring by the U.S. Government or any agency thereof. The views and opinions of authors expressed herein do not necessarily state or reflect those of the U.S. Government or any agency thereof.

This material is based upon work supported by the Department of Energy National Nuclear Security Administration under Award Number DE-NA0003856 and US National Science Foundation PHY Grant No. 1802964. This research used resources of the National Energy Research Scientific Computing Center, a DOE Office of Science User Facility supported by the Office of Science of the U.S. Department of Energy under Contract No. DE-AC02-05CH11231.

[1] J.J. Fortney and N. Nettelmann, "The Interior Structure, Composition, and Evolution of Giant Planets", Space Sci. Rev. **152**, 423-447 (2010).
[2] S.X. Hu, B. Militzer, V.N. Goncharov, and S. Skupsky, "First-principles equation-of-state table of deuterium for inertial confinement fusion applications", Phys. Rev. B **84**, 224109(1-18) (2011).
[3] S.X. Hu, L.A. Collins, V.N. Goncharov, T.R. Boehly, R. Epstein R.L. McCrory, and S. Skupsky, "First-principles opacity table of warm dense deuterium for inertial-confinement-fusion applications", Phys. Rev. E **90**, 033111(1-10) (2014).
[4] S.X. Hu, V.N. Goncharov, T.R. Boehly, R.L. McCrory, S. Skupsky, L.A. Collins, J.D. Kress, and B. Militzer, "Impact of first-principles properties of deuteriumtritium on inertial confinement fusion target designs", Phys. Plasmas **22**, 056304 (2015).
[5] A. Fernandez-Pañella, M. Millot, D.E. Fratanduono, M. Desjarlais, S. Hamel, M.C. Marshall, D.J. Erskine, P.A. Sterne, S. Haan, T.R. Boehly, G.W. Collins, J.H. Eggert and P.M. Celliers, "Shock compression of liquid deuterium up to 1 TPa", Phys. Rev. Lett. (2019) (in press).
[6] M.D. Knudson, and M.P. Desjarlais, Phys. Rev. Lett. **118**, 035501 (2017).
[7] N.D. Mermin, Phys. Rev. **137**, A1441 (1965).
[8] M.V. Stoitsov and I.Zh. Petkov, Annals Phys. **185**, 121 (1988).
[9] R.M. Dreizler in *The Nuclear Equation of State, Part A*, W. Greiner and H. Stöcker eds., NATO ASI B**216** (Plenum, NY, 1989) 521.
[10] N.M. Tubman, E. Liberatore, C. Pierleoni, M. Holzmann, and D.M. Ceperley, Phys. Rev. Lett. **115**, 045301 (2015).
[11] M. Dion, H. Rydberg, E. Schröder, D.C. Langreth, and B.I. Lundqvist, Phys. Rev. Lett. **92**, 246401 (2004).
[12] K. Lee, E.D. Murray, L. Kong, B.I. Lundqvist, and D.C. Langreth, Phys. Rev. B **82**, 081101(R) (2010).
[13] J.P. Perdew, K. Burke, and M. Ernzerhof, Phys. Rev. Lett. **77**, 3865 (1996); erratum *ibid.* **78**, 1396 (1997).
[14] R. Kubo, J. Phys. Soc. Jpn. **12**, 570 (1957).
[15] D.A. Greenwood, Proc. Phys. Soc. **71**, 585 (1958).
[16] Y.T. Lee and R.M. More, Phys. Fluids **27**, 1273 (1984).
[17] B. Wilson, V. Sonnad, P. Sterne, and W. Isaacs, J. Quant. Spectrosc. Radiat. Transfer **99**, 658 (2006).
[18] B. Holst, R. Redmer, and M.P. Desjarlais, Phys. Rev. B **77**, 184201 (2008).
[19] L. Caillabet, S. Mazevet, and P. Loubeyre, Phys. Rev. B **83**, 094101 (2011).
[20] L.A. Collins, S.R. Bickham, J.D. Kress, and S. Mazevet, T.J. Lenosky, N.J. Troullier, W. Windl, Phys. Rev. B **63**, 184110 (2001).
[21] L.A. Collins, J.D. Kress, and D.E. Hanson, Phys. Rev. B **85**, 233101 (2012).
[22] V.V. Karasiev, L. Calderín, and S.B. Trickey, Phys. Rev. E **93**, 063207 (2016).
[23] V.V. Karasiev, S.B. Trickey, and J.W. Dufty, Phys. Rev. B **99**, 195134 (2019).
[24] V.V. Karasiev, J.W. Dufty, and S.B. Trickey, "Nonempirical Semilocal Free-Energy Density Functional for Matter under Extreme Conditions", Phys. Rev. Lett. **120**, 076401(1-7) (2018).
[25] V.V. Karasiev, T. Sjostrom, J. Dufty, and S.B. Trickey, Phys. Rev. Lett. **112**, 076403 (2014).
[26] J.P. Perdew, and A. Zunger, Phys. Rev. B **23**, 5048 (1981).
[27] R.P. Feynman, N. Metropolis, and E. Teller, Phys. Rev. **75**, 1561 (1949).
[28] V.V. Karasiev, T. Sjostrom, and S.B. Trickey, Comput. Phys. Commun. **185**, 3240 (2014).
[29] G.S. Ho, V.L. Lignères, and E.A. Carter, Comput. Phys. Commun. **179**, 839 (2008).

[30] L. Hung, C. Huang, I. Shin, G.S. Ho, V.L. Lignères, and E.A. Carter, Comput. Phys. Commun. **181**, 2208 (2010).

[31] P. Giannozzi, Paolo Giannozzi, Stefano Baroni, Nicola Bonini, Matteo Calandra, Roberto Car, Carlo Cavazzoni, Davide Ceresoli, Guido L. Chiarotti, Matteo Cococcioni, Ismaila Dabo, Andrea Dal Corso, Stefano de Gironcoli, Stefano Fabris, Guido Fratesi, Ralph Gebauer, Uwe Gerstmann, Christos Gougoussis, Anton Kokalj, Michele Lazzeri, Layla Martin-Samos, Nicola Marzari, Francesco Mauri, Riccardo Mazzarello, Stefano Paolini, Alfredo Pasquarello, Lorenzo Paulatto, Carlo Sbraccia, Sandro Scandolo, Gabriele Sclauzero, Ari P. Seitsonen, Alexander Smogunov, Paolo Umari, and Renata M. Wentzcovitch, "QUANTUM ESPRESSO: a Modular and Open-Source Software Project for Quantum Simulations of Materials", J. Phys.: Condens. Matter **21**, 395502(1-19) (2009).

[32] F. Jollet, M. Torrent, N. Holzwarth, Comput. Phys. Commun. **185**, 1246 (2014).

[33] V.V. Karasiev, T. Sjostrom, and S.B. Trickey, Phys. Rev. B **86**, 115101 (2012).

[34] V.V. Karasiev, T. Sjostrom, and S.B. Trickey, Phys. Rev. E **86**, 056704 (2012).

[35] A. Baldcreschi, Phys. Rev. B **7**, 5212 (1973).

[36] X. Gonze, B. Amadon, P.-M. Anglade, J.-M. Beuken, F. Bottin, P. Boulanger, F. Bruneval, D. Caliste, R. Caracas, M. Cote, T. Deutsch, L. Genovese, Ph. Ghosez, M. Giantomassi, S. Goedecker, D.R. Hamann, P. Hermet, F. Jollet, G. Jomard, S. Leroux, M. Mancini, S. Mazevet, M.J.T. Oliveira, G. Onida, Y. Pouillon, T. Rangel, G.-M. Rignanese, D. Sangalli, R. Shaltaf, M. Torrent, M.J. Verstraete, G. Zerah, and J.W. Zwanziger, Comput. Phys. Commun. **180**, 2582 (2009); X. Gonze, G.-M. Rignanese, M. Verstraete, J.-M. Beuken, Y. Pouillon, R. Caracas, F. Jollet, M. Torrent, G. Zerah, M. Mikami, Ph. Ghosez, M. Veithen, J.-Y. Raty, V. Olevano, F. Bruneval, L. Reining, R. Godby, G. Onida, D.R. Hamann, and D.C. Allan, Zeit. Kristallogr. **220**, 558 (2005).

[37] S. Mazevet, M. Torrent, V. Recoules, and F. Jollet, High Energy Density Phys. **6**, 84 (2010).

[38] L. Calderín, V.V. Karasiev, and S.B. Trickey, Comput. Phys. Commun. **221**, 118-142 (2017).

[39] M.P. Desjarlais, J.D. Kress, and L.A. Collins, Phys. Rev. E **66**, 025401(R) (2002).

[40] S. Mazevet, L.A. Collins, N.H. Magee, J.D. Kress, and J.J. Keady, Astron. Astrophys. **405**, L5 (2003).

[41] S. Mazevet, J.D. Kress, and L.A. Collins, and P. Blottiau, Phys. Rev. B **67**, 054201 (2003).

[42] S. Mazevet, M.P. Desjarlais, L.A. Collins, J.D. Kress, and N.H. Magee, Phys. Rev. E **71**, 016409 (2005).

[43] V. Recoules, and J.-P. Crocombette, Phys. Rev. B **72**, 104202 (2005).

[44] H.J. Monkhorst and J.D. Pack, Phys. Rev. B **13**, 5188 (1976).

[45] G.I. Kerley, "Equations of state for hydrogen and deuterium", Sandia National Laboratories Technical Report No. SAND2003-3613, 2003, doi:10.2172/917468.

[46] P.C. Soures, "*Hydrogen Properties for Fusion Energy*", University of California Press, Berkeley, (1986).

[47] M. Zaghoo, T.R. Boehly, J.R. Rygg, P.M. Celliers, S.X. Hu, and G.W. Collins, Phys. Rev. Lett. **122**, 085001 (2019)

[48] P.M. Celliers, G.W. Collins, L.B. Da Silva, D.M. Gold, R. Cauble, R.J. Wallace, M.E. Foord, and B.A. Hammel, Phys. Rev. Lett. **84**, 5564 (2000).

[49] *The Pade Approximant in Theoretical Physics*, G.A. Baker Jr. and J.L. Gammel (Academic Press, NY, 1970).

[50] D. Mejia-Rodriguez, and S.B. Trickey, Phys. Rev. A **96**, 052512 (2017).

[51] J. Hinz, V.V. Karasiev, S.X. Hu, M. Zaghoo, and D. Mejia-Rodriguez, "Deorbitalized meta-GGA with the long-range van der Waals exchange-correlation functional calculations of the insulator-metal transition of hydrogen", Poster presentation at the 59th Sanibel Simposium, Feb. 17–22, 2019, St. Simon Island.